

# Search for supersymmetry in diphoton final states with the CMS detector

Matthew Lawrence Joyce

February 25, 2021

## CONTENTS

1.	<i>The Standard Model</i>	6
2.	<i>Supersymmetry</i>	7
3.	<i>The Large Hadron Collider</i>	8
3.1	Introduction	8
3.2	Injection Complex	8
3.3	Tunnel and Magnets	9
3.4	Luminosity	11
4.	<i>Compact Muon Solenoid</i>	13
4.1	Introduction	13
4.2	Coordinate System	14
4.3	Superconducting Magnet	15
4.4	Tracker	15
4.4.1	Pixel Detector	15
4.4.2	Strip Detector	16
4.5	Electromagnetic Calorimeter	17
4.5.1	Crystals	18
4.5.2	Barrel and Endcaps	19
4.5.3	Preshower layer	20
4.5.4	Performance	20
4.6	Hadronic Calorimeter	21
4.7	Superconducting Solenoid	22
4.8	Muon System	22
5.	<i>MIP Timing Detector (MTD)</i>	25
5.1	Introduction	25
5.2	Barrel Timing Layer	26

## LIST OF FIGURES

3.1	LHC interaction points . . . . .	9
3.2	Layout of LHC accelerator complex [14]. . . . .	10
3.3	Proton bunch capture onto RF bucket [5]. . . . .	11
3.4	Cross section of LHC dipole [7] . . . . .	12
3.5	Integrated luminosity delivered by the LHC to the CMS experiment each year from 2010-2018. . . . .	12
4.1	Schematic of CMS detector [15] . . . . .	13
4.2	Transverse slice of the CMS detector[6]. . . . .	14
4.3	Cross section (side) of CMS tracker prior to the Phase 1 upgrade during the year-end technical stop of 2016/2017. Each line represents a detector module while double lines indicate back-to-back strip modules. Surrounding the pixel tracker (PIXEL) is the strip detector, which is divided into the Tracker Inner Barrel (TIB), Tracker Outer Barrel (TOB), Tracker Inner Disks (TID), and Tracker Endcaps (TEC). Reprinted from Reference [10]. . . . .	16
4.4	Cross section (side) of pixel detector. The lower half , labeled "Current", shows the design prior to 2017 while the upper half, labeled "Upgrade", shows the design after the upgrade. Reprinted from Resource [9] . . . . .	17
4.5	PbWO <sub>4</sub> crystals. Left: EB crystal with APD. Right: EE crystal with VPT. Reprinted from [11] . . . . .	19
4.6	Schematic of ECAL. Reprint from [11] . . . . .	20
4.7	Longitudinal view of HCAL [2] . . . . .	22
4.8	Longitudinal slice of CMS detector while operating at 3.8-T central magnetic field. The right-hand side of the figure shows a mapping of the magnetic field lines while the left-hand side shows a mapping of the field strength. Reprint from [8] . . .	23

4.9	Cross-section of one quadrant of the CMS detector. The DTs are labeled as "MB" (Muon Barrel) and the CSCs are labelled as "ME" (Muon Endcap). The RPCs are "RB" for those in the barrel and "RE" for those in the endcap. Reprint from [16].	24
5.1	Timeline for LHC . . . . .	25
5.2	Vertices from a simulated 200 pileup event. Need to replace this with the figure from the TDR. . . . .	26

## LIST OF TABLES

4.1 Summary of signals expected for each particle type in each sub-detector. . . . .	14
---	----

## 1. THE STANDARD MODEL

## 2. SUPERSYMMETRY

3                   3. THE LARGE HADRON COLLIDER

4                   3.1 *Introduction*

5     The Large Hadron Collider (LHC) is a 26.7 kilometer-long, two-ring particle  
6     accelerator and collider located on the border of France and Switzerland at  
7     the European Organization for Nuclear Research (CERN). During normal  
8     operations the LHC maintains two counter-rotating beams of proton bunches  
9     that collide at four interaction points (IP) with up to  $\sqrt{s} = 14$  TeV center  
10    of mass energy and a luminosity of  $10^{34}\text{cm}^{-2}\text{s}^{-1}$ . The ALICE (Point 2),  
11    ATLAS (Point 1), CMS (Point 5), and LHC-b experiments each have a  
12    detector at one of these interaction points as scene in Figure 3.1 . The CMS  
13    and ATLAS are general-purpose detectors while LHC-b specializes in beauty  
14    quark studies. ALICE is a heavy-ion experiment which uses  $^{208}\text{Pb} - p$  or  
15     $^{208}\text{Pb} - ^{208}\text{Pb}$  collisions that can also be produced by the LHC.

16                  3.2 *Injection Complex*

17    In order to bring the protons from rest up to their target collision energy  
18    a series of accelerators, as shown in Figure 3.2, are used. The acceleration  
19    sequence begins with the injection of hydrogen gas into a duoplasmatron.  
20    Here a bombardment of electrons ionize the hydrogen atoms while an electric  
21    field pushes them through the duoplasmatron cavity. The result is 100 keV  
22    protons being passed on to a quadrupole magnet which guides them into  
23    the aperture of a linear accelerator (LINAC2). The radio frequency (RF)  
24    cavities in LINAC2 accelerate the protons up to 50 MeV. At this point the  
25    protons are sent into one of four rings in the Proton Synchrotron Booster  
26    (PSB). The PSB repeatedly accelerates the protons around a circular path  
27    until they reach an energy of 1.4 GeV. The bunches of protons from each PSB  
28    ring are then sequentially injected into the single-ringed Proton Synchrotron  
29    (PS). Each bunch injected into the PS are captured by one of the "buckets"  
30    (Figure 3.3) provided by the PS RF system which also manipulates the  
31    bunches into the desired profile and proton density. These proton bunches  
32    are accelerated to 25 GeV and injected into the Super Proton Synchrotron

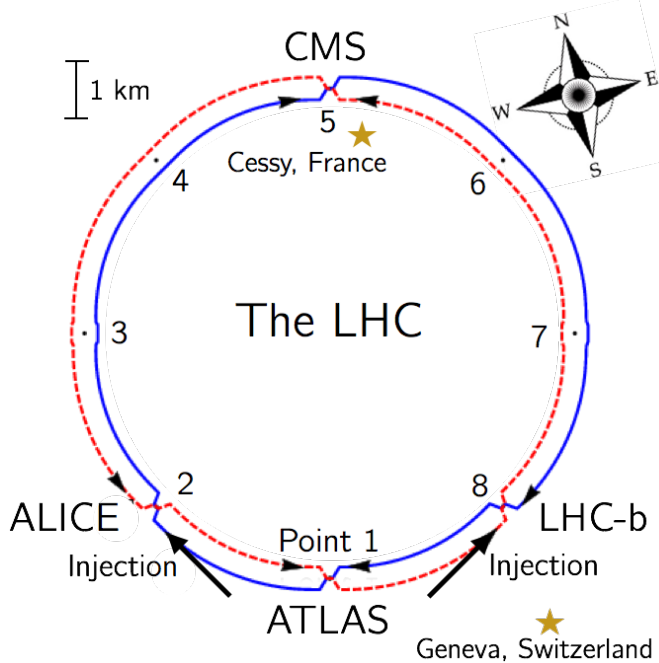


*Fig. 3.1:* Interaction points of the LHC

<sup>33</sup> (SPS) where they are accelerated to 450 GeV. Finally the proton bunches  
<sup>34</sup> are injected into the LHC ring where they are accelerated to 6.5 TeV and  
<sup>35</sup> collided in 25 ns intervals to yield a center of mass energy of  $\sqrt{s} = 13$  TeV.

### <sup>36</sup> 3.3 Tunnel and Magnets

<sup>37</sup> The LHC was designed to produce collisions with up to  $\sqrt{s} = 14$  TeV. That  
<sup>38</sup> requires confining and guiding 7 TeV protons around the circumference of  
<sup>39</sup> the LHC ring. The ring is housed in a 4 meter-wide underground tunnel  
<sup>40</sup> that ranges in depth between 45 and 170 meters below the surface. This  
<sup>41</sup> tunnel was repurposed from the Large Electron-Positron (LEP) Collider  
<sup>42</sup> which previously occupied the space. For this reason the tunnel is not  
<sup>43</sup> completely circular but is instead made up of alternating curved and straight  
<sup>44</sup> sections of 2500 m and 530 m in length respectively. The straight sections,  
<sup>45</sup> labeled 1-8 in Figure 3.1, are used as either experimental facilities or sites for  
<sup>46</sup> hardware necessary for LHC operations such as RF cavities for momentum  
<sup>47</sup> cleaning, quadrupole magnets for beam focusing, and sextupole magnets for  
<sup>48</sup> acceleration and betatron cleaning.

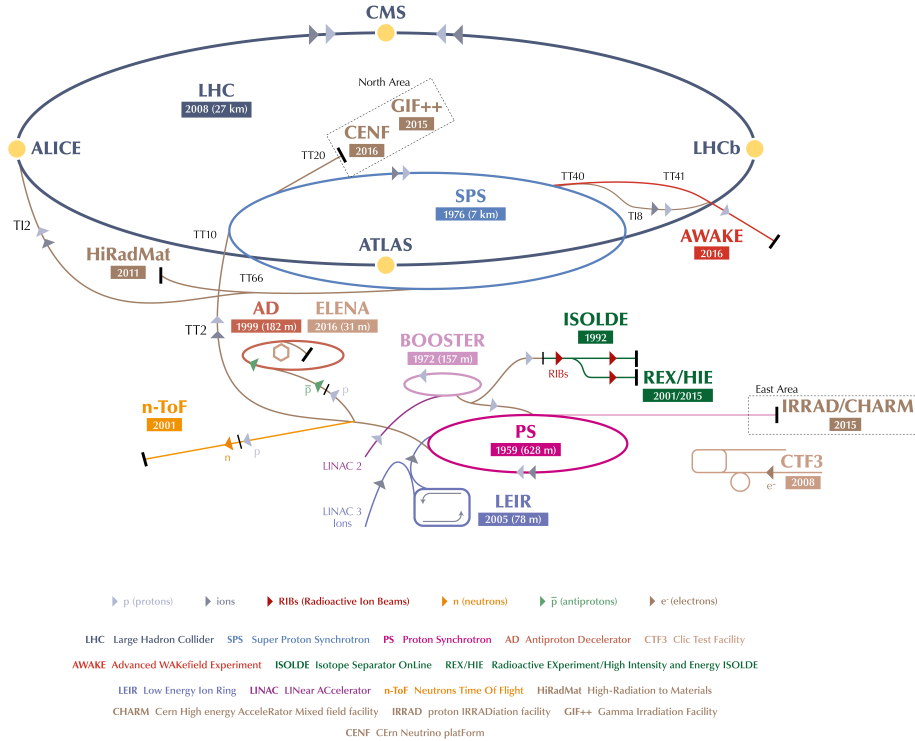


Fig. 3.2: Layout of LHC accelerator complex [14].

49     Steering a 7 TeV proton beam around the curved sections requires a mag-  
50     netic field of 8.33 Tesla which is provided by 1223 superconducting dipole  
51     magnets cooled to 1.9 K. A cross section of the LHC dipole is shown in  
52     Figure 3.4. Supercooled liquid helium flows through the heat exchanger  
53     pipe to cool the iron yolk to a temperature of 1.9 K. Ultra high vacuum  
54     is maintained in the outer volume to provide a layer of thermal insulation  
55     between the inner volume and the outer steel casing. Inside the iron yolk is a  
56     twin bore assembly of niobium-titanium superconducting coils. Two parallel  
57     beam pipes are located within the focus of the superconducting coils. This  
58     is the ultra high vacuum region where the subatomic particles are confined  
59     as they travel around the LHC ring.

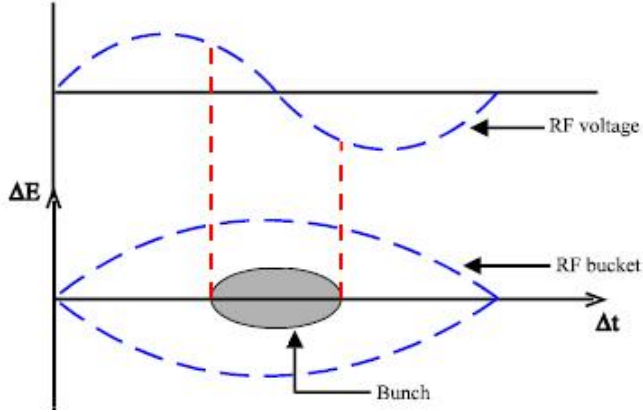


Fig. 3.3: Proton bunch capture onto RF bucket [5].

#### 3.4 Luminosity

60     The number of events generated per second for specific process having cross-  
61     section  $\sigma_{event}$  is given by:

$$\frac{dN_{event}}{dt} = L\sigma_{event} \quad (3.1)$$

63     where  $L$  in the machine luminosity. The machine luminosity for a Gaussian  
64     beam distribution can be written in terms of the beam parameters as:

$$L = \frac{N_b^2 n_b f_{rev} \gamma_r}{4\pi \epsilon_n \beta_*} F \quad (3.2)$$

65     where  $N_b$  is particle density in each bunch,  $n_b$  is the number of bunches  
66     in each beam,  $f_{rev}$  is the frequency of revolution, and  $\gamma_r$  is the relativistic  
67     gamma factor. The variables  $\epsilon_n$  and  $\beta_*$  are the normalized transverse beam  
68     emittance and the beta function at the IP respectively, while  $F$  is the geo-  
69     metric reduction factor depending due to the beams' crossing angle at the  
70     IP. [14]

71     The total number of events produced over a given amount of time would  
72     then be

$$N_{event} = \sigma_{event} \int L dt = \sigma_{event} L_{integrated}. \quad (3.3)$$

73     The integrated luminosity delivered each year to the CMS experiment is  
74     shown in 3.5. The analysis presented here uses data collected from the 2016,  
75     2017, and 2018 campaigns which gives a combined integrated luminosity of  
76      $158.7 \text{ fb}^{-1}$ .

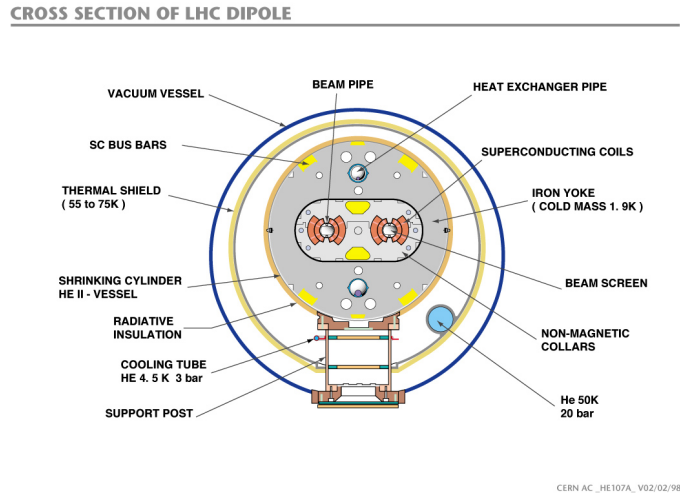


Fig. 3.4: Cross section of LHC dipole [7]

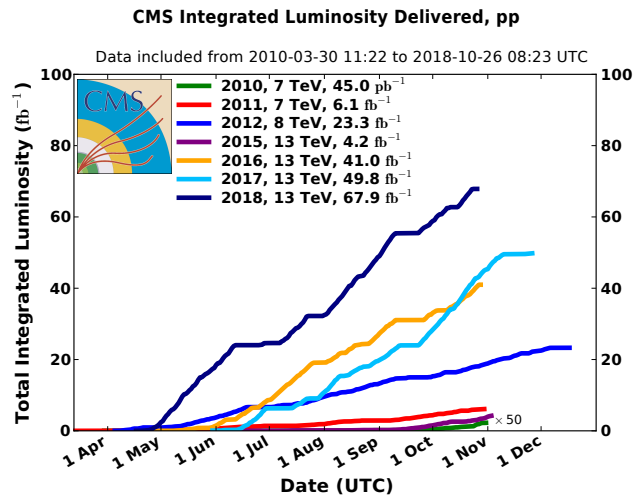
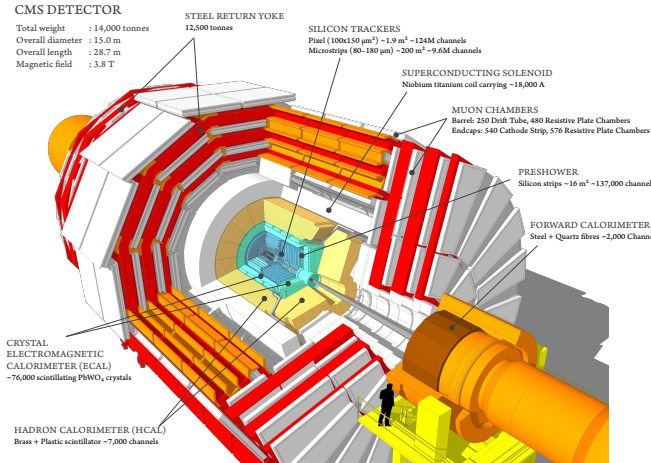


Fig. 3.5: Integrated luminosity delivered by the LHC to the CMS experiment each year from 2010-2018.

## 4. COMPACT MUON SOLENOID

### 4.1 Introduction

79 About 100 meters below the town of Cessy, France at Point 5 is the Compact  
 80 Muon Solenoid (CMS). The CMS is a general purpose detector weighing  
 81 14,000 tonnes with a length of 28.7 meters and a 15.0-meter diameter that  
 82 was designed to accurately measure the energy and momentum of particles  
 83 produced in the proton-proton or heavy-ion collisions at the LHC [11]. A  
 84 perspective view of the detector is shown in Figure 4.1. In order to get  
 85 a full picture of what is being produced by the collisions the CMS detector  
 86 must be able identify the resulting particles as well as accurately measure  
 87 their energy and momentum. For this reason the detector was designed to  
 88 be a collection of specialized sub-detectors, each of which contributes data  
 used in the reconstruction of a collision.



*Fig. 4.1: Schematic of CMS detector [15]*

90 At the heart of the CMS detector is a 3.8-Tesla magnetic field produced  
 91 by a superconducting solenoid. Inside the 6-meter diameter solenoid are

three layers of sub-detectors. These make up the inner detector and are, in order from innermost to outermost, the silicon tracker, the electromagnetic calorimeter (ECAL), and the hadronic calorimeter (HCAL). Outside the solenoid is the muon system. A transverse slice of the detector (Figure 4.2) shows the sub-detectors and how different types of particles interact with them. Table 4.1 shows a summary of which sub-detectors are expected to produce signals for different types of particles.

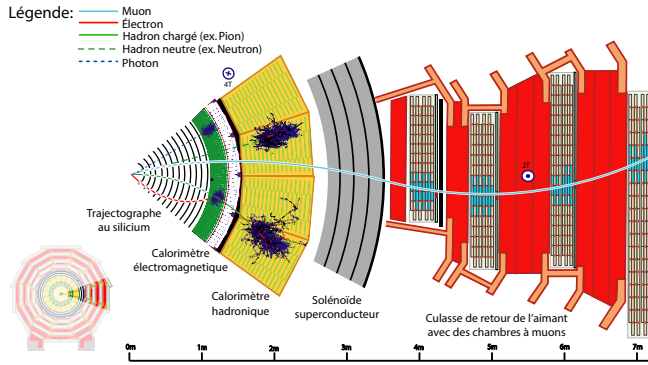


*Fig. 4.2:* Transverse slice of the CMS detector[6].

Particle	Tracker	ECAL	HCAL	Muon
Photons	No	Yes	No	No
Electrons	Yes	Yes	No	No
Hadrons (charged)	Yes	Yes	Yes	No
Hadrons (neutral)	No	No	Yes	No
Muons	Yes	Yes	Yes	Yes
Invisible ( $\nu$ , SUSY, etc)	No	No	No	No

*Tab. 4.1:* Summary of signals expected for each particle type in each sub-detector.

## 4.2 Coordinate System

The origin of the coordinate system used by CMS is centered at the nominal collision point in the center of the detector. A right-handed Cartesian system is used with the x-axis pointing radially inward toward the center of the LHC ring, y-axis pointing vertically upward, and the z-axis pointing tangent to

104 the LHC ring in the counterclockwise direction as viewed from above. CMS  
 105 also uses an approximately Lorentz invariant spherical coordinate system  
 106 spanned by three basis vectors. They are the transverse momentum  $p_T$ ,  
 107 pseudorapidity  $\eta$ , and azimuthal angle  $\phi$ . The transverse momentum and  
 108 azimuthal angle translate to the Cartesian system in the following ways  
 109 using the x and y-components of the linear momentum:

$$p_T = \sqrt{(p_x)^2 + (p_y)^2} \quad (4.1)$$

110

$$\phi = \tan^{-1} \frac{p_y}{p_x} \quad (4.2)$$

111 while the pseudorapidity can be translated using the polar angle  $\theta$  relative  
 112 the positive z-axis as

$$\eta = -\ln[\tan \frac{\theta}{2}]. \quad (4.3)$$

### 113 4.3 Superconducting Magnet

### 114 4.4 Tracker

115 The innermost sub-detector in CMS is the silicon tracker. The tracker is  
 116 used to reconstruct tracks and vertices of charged particles. In order to give  
 117 precise reconstruction of charged particle trajectories it needs to be position  
 118 as close as possible to the IP and have high granularity. The close proximity  
 119 to the IP requires the materials to be tolerant to the high levels of radiation  
 120 in that region. Being the innermost sub-detector it must also minimally  
 121 disturb particles as they pass through it into the other sub-detectors. These  
 122 criteria led to the design of the tracker using silicon semiconductors.

123 The silicon tracker is made up of two subsystems, an inner pixel detector  
 124 and an outer strip tracker which are oriented in a cylindrical shape with an  
 125 overall diameter of 2.4 m and length of 5.6 m centered on the interaction  
 126 point. Both subsystems consist of barrel and endcap regions which can be  
 127 seen in Figure 4.3.

#### 128 4.4.1 Pixel Detector

129 The pixel detector is the innermost subsystem in the silicon tracker and  
 130 spans the pseudorapidity range  $|\eta| < 2.5$  and is responsible for small im-  
 131 pact parameter resolution which is important for accurate reconstruction of  
 132 secondary vertices [11]. In order to produce these precise measurements a  
 133 very high granularity is required. In addition to this the proximity to the

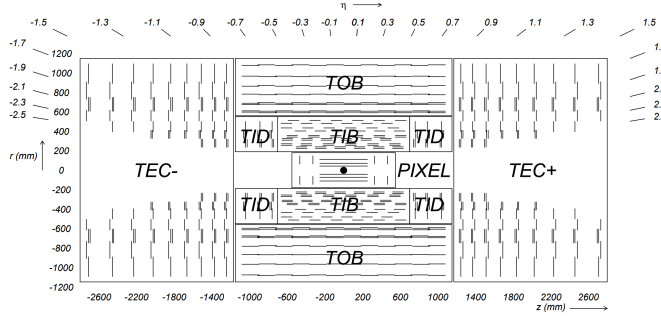


*Fig. 4.3:* Cross section (side) of CMS tracker prior to the Phase 1 upgrade during the year-end technical stop of 2016/2017. Each line represents a detector module while double lines indicate back-to-back strip modules. Surrounding the pixel tracker (PIXEL) is the strip detector, which is divided into the Tracker Inner Barrel (TIB), Tracker Outer Barrel (TOB), Tracker Inner Disks (TID), and Tracker Endcaps (TEC). Reprinted from Reference [10].

134 IP means that one expects there to be high occupancy of the tracker. These  
135 constraints are met by using pixels with a cell size of  $100 \times 150 \mu\text{m}^2$ .

136 The original pixel detector was designed for operation at the nominal  
137 instantaneous luminosity of  $10^{34} \text{ cm}^{-2}\text{s}^{-1}$  with 25 ns between proton bunch  
138 crossings, resulting in on average about 25 proton-proton interactions occur-  
139 ring per bunch crossing or pileup [10]. During the LHC technical shutdown  
140 of 2016/17, the pixel detector underwent the scheduled Phase 1 upgrade  
141 which would allow operation at higher levels of instantaneous luminosity  
142 and pileup. Figure 4.4 shows a cross sectional view in the  $r$ - $z$  plane. Prior  
143 to 2017 there were three barrel layers and two endcap layers on each side  
144 which provide three very precise space points for each charged particle. The  
145 upgrade decreased the radius of the innermost barrel layer from 4.4 cm to  
146 3.0 cm and added a fourth barrel layer as well as adding third endcap layer  
147 to each side. Each of the endcap layers consisted of two half-disks populated  
148 with pixel modules whereas the upgraded endcap layers were split into inner  
149 and outer rings. [9]

#### 150 4.4.2 Strip Detector

151 The silicon strip detector surrounds the pixel detector and is comprised of  
152 four subsystems, the Tracker Inner Barrel (TIB), the Tracker Outer Barrel  
153 (TOB), the Tracker Inner Disks (TID), and the Tracker Endcaps (TEC),  
154 all of which can be seen in Figure 4.3 [11]. The TIB and TID both use

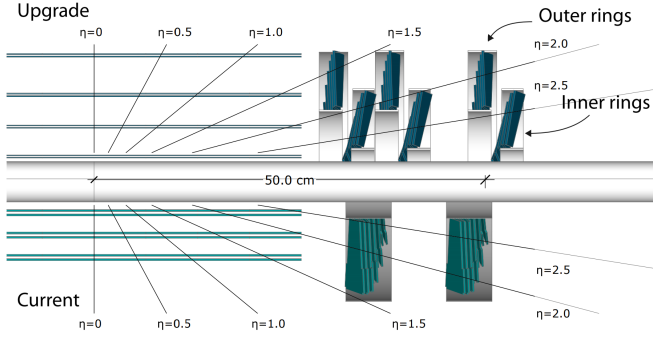


*Fig. 4.4:* Cross section (side) of pixel detector. The lower half , labeled "Current", shows the design prior to 2017 while the upper half, labeled "Upgrade", shows the design after the upgrade. Reprinted from Resource [9]

155 320  $\mu\text{m}$  thick silicon micro-strip sensors oriented along  $z$  and  $r$  respectively.  
 156 The TIB has four layers while the TID is composed of three layers. This  
 157 geometry allows the TIB and TID to combine to provide up to four  $r - \phi$   
 158 measurements on charged particle trajectories.

159 Surrounding the TIB and TID is the TOB, which extends between  $z \pm 118$   
 160 cm. This subsystem consists of six layers of 500  $\mu\text{m}$  thick silicon micro-strip  
 161 sensors with strip pitches ranging from 122  $\mu\text{m}$  to 183  $\mu\text{m}$ , providing six  
 162 more  $r - \phi$  measurements in addition to those from the TIB/TID subsystems.  
 163 Beyond the  $z$  range of the TOB is the TEC. Each TEC is made up of nine  
 164 disks. Each of the nine disks has up to seven concentric rings of micro-strip  
 165 sensors oriented in radial strips with those on the inner four rings being  
 166 320  $\mu\text{m}$  thick and the rest being 500  $\mu\text{m}$  thick, providing up to nine  $\phi$   
 167 measurements for the trajectory of a charged particle.

168 To provide additional measurements of the  $z$  coordinate in the barrel and  
 169  $r$  coordinate in the disks a second micro-strip detector module is mounted  
 170 back-to-back with stereo angle 100 mrad in the first two layers of the TIB  
 171 and TOB, the first two rings of the TID, and rings 1, 2, and 5 of the TEC.  
 172 The resulting single point resolution is 230  $\mu\text{m}$  in the TIB and 530  $\mu\text{m}$  in the  
 173 TOB. The layout of these subsystems ensures at least nine hits for  $|\eta| < 2.4$   
 174 with at least four of hits yielding a 2D measurement.

## 175 4.5 Electromagnetic Calorimeter

176 The electromagnetic calorimeter (ECAL) lies just outside the tracker and is a  
 177 hermetic homogeneous calorimeter designed to measure the energy deposited

178 by electrons and photons. It consists of a central barrel (EB) with 61200  
179 lead tungstate ( $\text{PbWO}_4$ ) crystals which is closed by two endcaps (EE), each  
180 having 7324 crystals. Highly-relativistic charged particles passing through a  
181 crystal primarily lose energy by producing bremsstrahlung photons. Photons  
182 lose energy by producing  $e^- - e^+$  pairs. In front of each EE is a preshower  
183 (ES) detector which acts as a two-layered sampling calorimeter. The crystals  
184 in the EB are instrumented with avalanche photodiodes (APDs) while the  
185 EE crystals are instrumented with vacuum phototriodes (VPTs). The ECAL  
186 design was strongly driven to be sensitive to the di-photon decay channel  
187 of the Higgs boson. This led to the design of a calorimeter that was fast,  
188 radiation-hard, and had good spatial and energy resolution.

189                   4.5.1 Crystals

190 In order to provide a good spacial resolution it was necessary for the ECAL  
191 to have a fine granularity. The small Molier radius (22 mm) and short radia-  
192 tion length (8.9 mm) of  $\text{PbWO}_4$  allows for fine granularity while maintaining  
193 good energy resolution by containing nearly all of the energy from an EM  
194 shower without the need for a restrictively thick crystal layer. The  $\text{PbWO}_4$   
195 scintillation is also fast enough that approximately 80 percent of an EM  
196 shower is produced within 25 ns, which is the also the amount of time be-  
197 tween bunch crossings at the LHC. These crystals have a Gaussian-shaped  
198 spectrum spanning from 360 nm to 570 nm with a maximum at approx-  
199 imately 440 nm. While  $\text{PbWO}_4$  is relatively radiation-hard, the amount  
200 of ionizing radiation seen by the crystal leading up to the HL-LHC era of  
201 operations causes wavelength-dependent degradation in light transmission.  
202 The scintillation mechanism however is unchanged so this damage can be  
203 tracked and accounted for by injecting laser light near the peak wavelength  
204 of the emission spectrum into the crystals to monitor optical transparency.

205 Light produced in the crystal is transmitted along its length and col-  
206 lected at the rear by either an APD in the EB or a VPT in one of the EE.  
207 Light output is temperature dependent so the crystals are kept at precisely  
208  $18^\circ\text{C}$  at which the yield is about 4.5 photoelectrons per MeV. The EB and  
209 EB crystals, which have a tuncated pyramidal shape to match the lateral de-  
210 velopment of the shower, along with their photosensors are shown in Figure  
211 4.5.

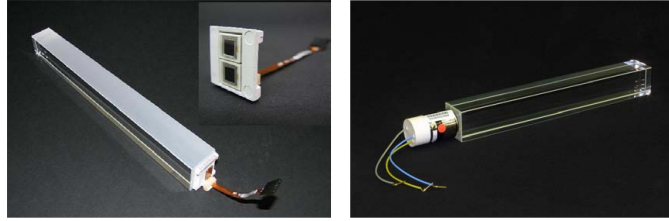


*Fig. 4.5:* PbWO<sub>4</sub> crystals. Left: EB crystal with APD. Right: EE crystal with VPT. Reprinted from [11]

212

#### 4.5.2 Barrel and Endcaps

213 The EB covers the pseudorapidity range  $|\eta| < 1.479$  and uses crystals that  
 214 are 230 mm long, which corresponds to 25.8 radiation lengths. The front  
 215 face of each crystal measures  $22 \times 22$  mm<sup>2</sup> while the rear face measures  $26 \times 26$   
 216 mm<sup>2</sup>. These are grouped in 36 supermodules (SM), each comprised of 1700  
 217 crystals arranged in a  $20 \times 85$  grid in  $\phi \times \eta$ . Each SM spans half the length  
 218 of the barrel and covers  $20^\circ$  in  $\phi$ . On the back face of each crystal is a  
 219 pair of APDs (semiconductor diodes). APDs are compact, immune to the  
 220 longitudinal 3.8 T magnetic field produced by the solenoid at this location,  
 221 and resistant to the radiation levels expected in the EB over a ten year  
 222 period. They also have high enough gain to counter to low light yield of  
 223 the crystals. All of this makes them an ideal choice for use in the EB. Each  
 224 APD has an active area of  $5 \times 5$  mm<sup>2</sup> and are operated at a gain of 50 which  
 225 requires a bias voltage between 340 and 430 V. As the gain of the APDs is  
 226 highly dependent on the applied bias voltage and any gain instability would  
 227 translate to degradation in energy resolution, very stable power supplies are  
 228 used to maintain voltages within a few tens of mV.

229 The EE cover the pseudorapidity range  $1.497 < |\eta| < 3.0$ . The crystals in  
 230 the EE have a  $28.62 \times 28.62$  mm<sup>2</sup> front face cross section and  $30 \times 30$  mm<sup>2</sup> rear  
 231 face cross section. Each crystal is 220 mm long which corresponds to 24.7  
 232 radiation lengths and are grouped in  $5 \times 5$  units called supercrystals (SCs).  
 233 Two halves, called *Dees*, make up each EE. Each Dee contains 138 SCs and  
 234 18 partial SCs which lie along the inner and outer circumference. On the  
 235 back of each crystal in EE is a VPT which is a conventional photomultiplier  
 236 with a single gain stage. While not as compact as the APDs used in the EB,  
 237 the VPTs are a more suitable for the more hostile environment at higher  
 238  $\eta$ . Each VPT has a 25-mm diameter and approximately 280 mm<sup>2</sup> of active  
 239 area. Though the VPT gain and quantum efficiency are lower than that of  
 240 the APDs this is offset by the larger active area allowing for better light

241 collection. Figure 4.6 shows the orientation of the crystals, modules, and  
 242 supermodules within the ECAL. [11]

243 **4.5.3 Preshower layer**

244 In front of each EE is a preshower (ES) detector. The main purpose of the  
 245 ES is to identify photons resulting from  $\pi^0 \rightarrow \gamma\gamma$  within the pseudorapidity  
 246 range  $1.653 < |\eta| < 2.6$ , but it also aids in the identification of electrons  
 247 against minimum ionizing particles (MIPs) and provides a spacial resolution  
 248 of 2 mm compared to the 3 mm resolution of the EB and EE. The ES acts  
 249 as a two-layered sampling calorimeter. Lead radiators make up the first  
 250 layer. These initiate electromagnetic showers from incoming electrons or  
 251 photons. The deposited energy and transverse profiles of these showers are  
 252 then measured by the silicon strip sensors which make up the second layer.

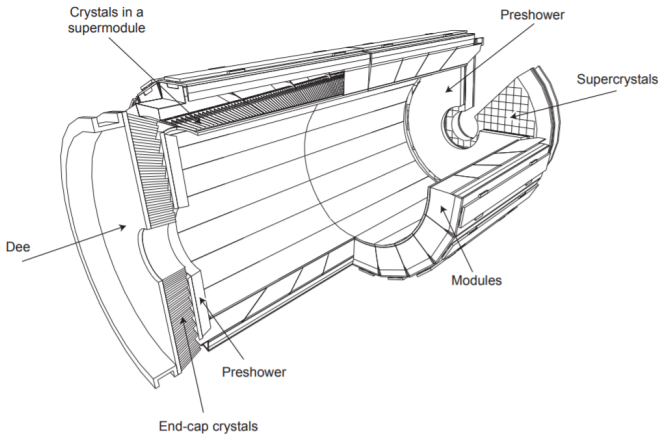


Fig. 4.6: Schematic of ECAL. Reprint from [11]

253 **4.5.4 Performance**

254 The energy resolution of the ECAL can be parameterized as

$$\frac{\sigma}{E} = \frac{S}{\sqrt{E}} \oplus \frac{N}{E} \oplus C \quad (4.4)$$

255 where  $S$  is the stochastic term characterizing the size of photostatistical  
 256 fluctuations,  $N$  is the term characterizing the contributions of electronic,  
 257 digital, and pileup noise, and  $C$  is a constant which accounts for crystal

258 performance non-uniformity, intercalibration errors, and leakage of energy  
 259 from the back of a crystal. The values for these terms, as measured in a  
 260 beam test using 20 to 250 GeV electrons, are  $S = 0.028 \text{ GeV}^{1/2}$ ,  $N = 0.12$   
 261 GeV, and  $C = 0.003$ . [11]

#### 262 4.6 Hadronic Calorimeter

263 In the space between the bore of the superconducting magnet and the ECAL  
 264 is the Hadronic Calorimeter (HCAL) [2]. The HCAL is a sampling calorime-  
 265 ter used for the measurement of hadronic jets and apparent missing trans-  
 266 verse energy resulting from neutrinos or exotic particles. It is made up of al-  
 267 ternating layers of plastic scintillator tiles and brass absorbers. EM showers  
 268 are generated by charged/neutral hadrons in the brass absorber. Charged  
 269 particles in the shower then produce scintillation light in the plastic scintil-  
 270 lator. Wavelength-shifting optical fibers embedded in the scintillator collect  
 271 and guide the scintillation light to pixelated hybrid photodiodes. A longi-  
 272 tudinal cross-section view in Figure 4.7 shows the geometric layout of the  
 273 HCAL’s barrel (HB), outer barrel (HO), endcap (HE), and forward (HF)  
 274 sections. The HB is comprised of 17 scintillator layers extending from 1.77  
 275 to 1.95 m and covers the pseudorapidity range of  $|\eta| < 1.4$ . The HO lies  
 276 outside the solenoid and is composed of only scintillating material. This  
 277 increases the interaction depth of the calorimeter system to a minimum of  
 278  $11\lambda_I$  for  $|\eta| < 1.26$  and thus reduces energy leakage. Also located inside  
 279 the solenoid are the two HE which cover pseudorapidities  $1.3 < |\eta| < 3.0$   
 280 and provide a thickness of  $10\lambda_I$ . In the forward region is the HF. This is  
 281 located 11.2 m away from the IP and covers the  $2.9 < |\eta| < 5.2$ . As the  
 282 HF is exposed to the highest levels of particle flux, it uses quartz fibers em-  
 283 bedded in steel absorbers rather than the materials used in the other parts  
 284 of the HCAL. Showers initiated by the absorbers produce Cerenkov light  
 285 in the quartz which transmits along to the fibers to photomultiplier tubes  
 286 (PMTs).

287 The HCAL inherently has lower energy resolution than the ECAL. A  
 288 large portion of the energy from hadronic showers is deposited in the ab-  
 289 sorbers and never makes it to the scintillation material. There are also  
 290 the possibilities that showers can be initiated prior to the particles reach-  
 291 ing HCAL or a charged particle could deposit energy in the ECAL through  
 292 bremsstrahlung. The combined energy resolution of the ECAL and the  
 293 HCAL barrels can be parameterized as

$$\frac{\sigma}{E} = \frac{S}{\sqrt{E}} \oplus C, \quad (4.5)$$

where  $E$  is the energy of the incident particle. These quantities were measured in a beam test using 2 to 350 GeV/c hadrons, electrons, and muons. The stochastic term is  $S = 0.847 \text{ GeV}^{1/2}$ , and the constant term is  $C = 0.074$  [3].

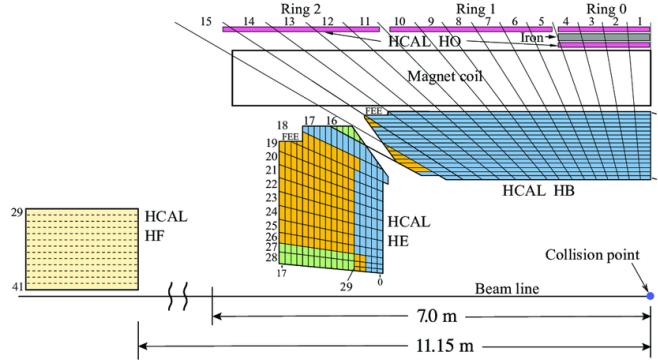


Fig. 4.7: Longitudinal view of HCAL [2]

#### 4.7 Superconducting Solenoid

In between the HCAL barrel and outer barrel is the superconducting solenoid magnet. The magnet is 12 m long with a 6-m inner diameter and provides the bending power necessary to precisely measure the momentum of charged particles. While it is capable of producing a 4 T magnetic field, the magnet is typically operated at 3.8 T. This is done to prolong the lifetime of the magnet. The Niobium Titanium coils used to create the uniform 3.8-T magnetic field are suspended in a vacuum cryostat and cooled by liquid helium to a temperature of 4.5 K. The magnet has a stored energy of 2.6 GJ when operating at full current. There are five wheels in the barrel and three disks on each endcap that make up a 12,000 ton steel yoke which serves to return the magnetic flux. This, along with a mapping of the calculated field strength, can be seen in Figure 4.8. More details on the superconducting solenoid magnet can be found at [1]

#### 4.8 Muon System

Embedded in magnet return yoke and encapsulating all of the other sub-detectors is the muon system. The muon system is the outermost layer

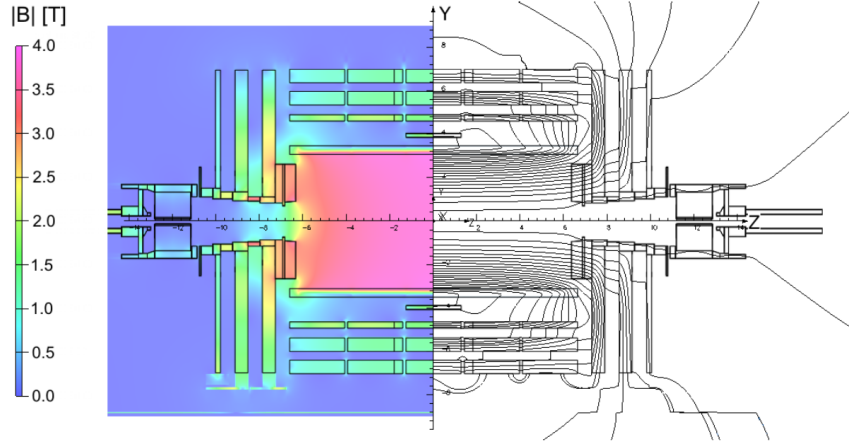


*Fig. 4.8:* Longitudinal slice of CMS detector while operating at 3.8-T central magnetic field. The right-hand side of the figure shows a mapping of the magnetic field lines while the left-hand side shows a mapping of the field strength. Reprint from [8]

because muons don't interact via the strong force and electromagnetic interactions alone are not enough stop them due to their large mass, therefore the only particles that are capable of making it to the muon system are muons and weakly-interacting particles such as neutrinos. The muon system is comprised of three different types of detectors. These are drift tube (DT) chambers, cathode strip chambers (CSC), and resistive plate chambers (RPC). A cross-sectional view of the muon system along with the rest of the CMS detector is shown in Figure 4.9.

The DT chambers are used barrel region for  $|\eta| < 1.2$ . Each chamber is comprised of three superlayers which are made up of four staggered layers of rectangular drift cells. Each of these drift cells contains a mixture of Ar and CO<sub>2</sub> gases. An anode wire, located at the center of each tube, is made of gold-plated stainless steel and is held at 3.6 kV. The gas is ionized when a charged particle passes through and the resulting free electrons are attracted to the anode wire. As these electrons pass through the gas they cause further ionization which results in an electron avalanche. The layers of drift cells are oriented in such a way that two of the three superlayers give the muon position in the  $\phi$ -direction and one gives the position in the  $z$ -direction. The result is a spacial resolution of 77-123  $\mu\text{m}$  along the  $\phi$  direction and 133-193  $\mu\text{m}$  along the  $z$  direction for each DT chamber [12].

On the endcaps, covering the pseudorapidity range of  $0.9 < |\eta| < 2.4$ ,

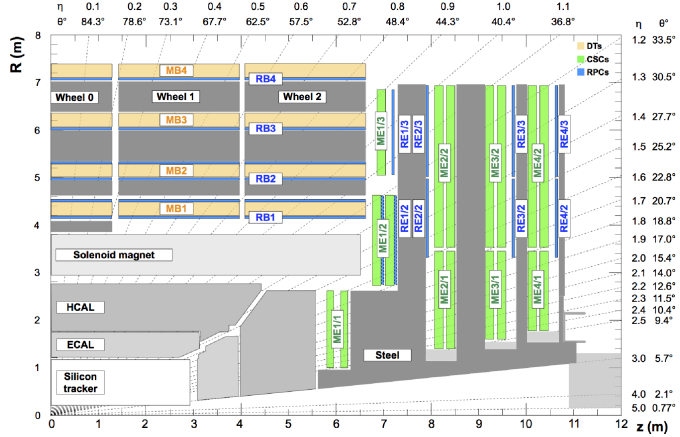


*Fig. 4.9:* Cross-section of one quadrant of the CMS detector. The DTs are labeled as "MB" (Muon Barrel) and the CSCs are labelled as "ME" (Muon Endcap). The RPCs are "RB" for those in the barrel and "RE" for those in the endcap. Reprint from [16].

336 are the CSCs. In this region there is a higher muon flux as well non-uniform  
 337 magnetic fields so this portion of the muon system must have higher gran-  
 338 ularity provided by the CSCs. Each of these chambers contain panels that  
 339 divide it into six staggered layers. The cathode strips are oriented along the  
 340  $r$ -direction to give position measurements in the  $\phi$ -direction while anode  
 341 wires run perpendicular in between the panels to give  $r$ -direction position  
 342 measurements. The spacial resolution provided by the CSCs is 45-143  $\mu\text{m}$   
 343 [16].

344 Both the endcap and barrel regions, spanning  $|\eta| < 1.6$ , contain RPCs to  
 345 provide more precise timing measurements. Each RPC is a gaseous parallel-  
 346 plate detector. High voltage is applied to two large plates which have a  
 347 layer of gas between them. Outside the chamber is an array of cathode  
 348 strips which is used to detect electron cascades resulting from muons passing  
 349 through and ionizing the gas. Where the DTs and CSCs provide precise  
 350 position information, the RPCs have a very fast response time which gives  
 351 a time resolution better than 3 ns [16]. This allows for the RPCs to be used  
 352 as a dedicated muon trigger that can insure each muon is assigned to the  
 353 correct bunch crossing.

## 5. MIP TIMING DETECTOR (MTD)

### 5.1 Introduction

356 In the coming years the LHC will be working toward upgrades that will  
 357 lead a substantial increase in luminosity. The timeline for future operations  
 358 of the LHC is shown in Figure 5.1. In 2019 the LHC entered a two-year  
 359 shutdown, Long Shutdown 2 (LS2). Upgrades of the LHC injector complex  
 360 to increase the beam brightness will take place during this shutdown. After  
 361 LS2 the LHC will enter Run 3 which will run for three years at 13-14 TeV. At  
 362 the completion of Run 3 the LHC will enter Long Shutdown 3 (LS3) which  
 363 will last approximately 2.5 years. During LS3 the optics in the interaction  
 364 region will be upgraded to produce smaller beams at the interaction point.  
 365 The completion of this upgrade will usher in the High Luminosity (HL-LHC)  
 366 era or Phase 2 of LHC operations, during which the combination of brighter  
 367 beams and a new focusing scheme at the IP allows for a potential luminosity  
 368 of  $2 \times 10^{35} \text{ cm}^{-2}\text{s}^{-1}$  at the beginning of each fill [4].

**LHC/ High-Luminosity LHC timeline**

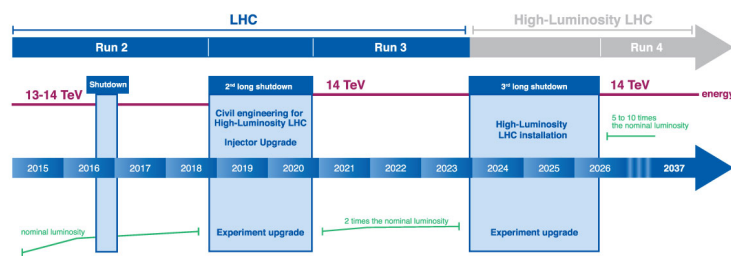


*Fig. 5.1: Timeline for LHC [13]*

369 The increased luminosity results in more interactions per bunch cross-  
 370 ing or pileup. In order to limit the amount of pileup the experiments must

disentangle to more manageable levels, the nominal scenario would be operating at a stable luminosity of  $5.0 \times 10^{34} \text{ cm}^{-2} \text{ s}^{-1}$ . This would limit the pileup to an average of 140. The ultimate scenario for operations would be running at  $7.5 \times 10^{34} \text{ cm}^{-2} \text{ s}^{-1}$  which brings the average pileup up to 200. The CMS detector in its current state is not capable of dealing with  $\approx 140\text{-}200$  pileup. At this level of pileup the spacial overlaps of tracks and energy depositions would lead to a degradation in the ability to identify and reconstruct hard interactions. In order to preserve the data quality of the current CMS detector this increased pileup must be reduced to an equivalent level approximately equal to current LHC operations which is  $\sim 40$ . The collision vertices within a bunch crossing have an RMS spread of 180-200 ps in time. If the beam spot were to be sliced into consecutive snap shots of 30-40 ps then the pileup levels per snapshot would be approximately 40. The space-time reconstruction of a 200 pileup event is shown in Figure 5.2. The addition of timing information to the  $z$  position spreads apart the vertices that would otherwise have been merged together and indiscernible. In order to achieve this a detector dedicated to the precise timing of minimum ionizing particles (MIPs), the MTD, will be added to the CMS detector.

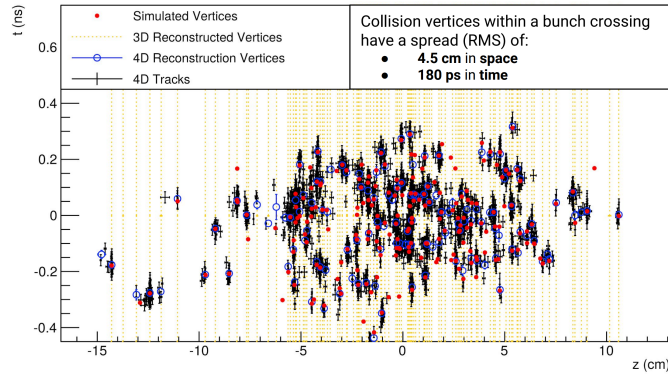


*Fig. 5.2:* Vertices from a simulated 200 pileup event. Need to replace this with the figure from the TDR.

389

## 5.2 Barrel Timing Layer

390 The Barrel Timing Layer (BTL) makes up the barrel region of the MTD.  
 391 It will provide pseudorapidity coverage up to  $|\eta| = 1.48$  with a geometric  
 392 acceptance of  $\sim 90\%$ . The BTL will be capable of detecting MIPs with a  
 393 time resolution of 30 ps at the start of Phase-2 operations and a luminosity-

<sup>394</sup> weighted time resolution of  $\sim 45$  ps when radiation damage effects are taken  
<sup>395</sup> into account.

## BIBLIOGRAPHY

- [1] *The CMS electromagnetic calorimeter project: Technical Design Report.* Technical design report. CMS. CERN, Geneva, 1997.
- [2] *The CMS hadron calorimeter project: Technical Design Report.* Technical design report. CMS. CERN, Geneva, 1997.
- [3] S. Abdullin et al. The CMS barrel calorimeter response to particle beams from 2-GeV/c to 350-GeV/c. *Eur. Phys. J. C*, 60:359–373, 2009. [Erratum: Eur.Phys.J.C 61, 353–356 (2009)].
- [4] G. Apollinari, O. Brüning, T. Nakamoto, and Lucio Rossi. High Luminosity Large Hadron Collider HL-LHC. *CERN Yellow Rep.*, (5):1–19, 2015.
- [5] S Baird. Accelerators for pedestrians; rev. version. Technical Report AB-Note-2007-014. CERN-AB-Note-2007-014. PS-OP-Note-95-17-Rev-2. CERN-PS-OP-Note-95-17-Rev-2, CERN, Geneva, Feb 2007.
- [6] David Barney. CMS Slice. Feb 2015.
- [7] Jean-Luc Caron. Cross section of lhc dipole.. dipole lhc: coupe transversale. ”AC Collection. Legacy of AC. Pictures from 1992 to 2002.”, May 1998.
- [8] S Chatrchyan et al. Precise Mapping of the Magnetic Field in the CMS Barrel Yoke using Cosmic Rays. *JINST*, 5:T03021, 2010.
- [9] CMS Collaboration. CMS Technical Design Report for the Pixel Detector Upgrade. Technical Report CERN-LHCC-2012-016. CMS-TDR-11, Sep 2012. Additional contacts: Jeffrey Spalding, Fermilab, Jeffrey.Spalding@cern.ch Didier Contardo, Universite Claude Bernard-Lyon I, didier.claude.contardo@cern.ch.
- [10] CMS Collaboration. Description and performance of track and primary-vertex reconstruction with the CMS tracker. *JINST*, 9(CMS-TRK-11-001. CERN-PH-EP-2014-070. CMS-TRK-11-001):P10009. 80 p, May

2014. Comments: Replaced with published version. Added journal reference and DOI.
- [11] The CMS Collaboration. The CMS experiment at the CERN LHC. *Journal of Instrumentation*, 3(08):S08004–S08004, aug 2008.
  - [12] The CMS collaboration. The performance of the CMS muon detector in proton-proton collisions at  $\sqrt{s}=7$  TeV at the LHC. *Journal of Instrumentation*, 8(11):P11002–P11002, nov 2013.
  - [13] Cinzia De Melis. Timeline for the LHC and High-Luminosity LHC. Frise chronologique du LHC et du LHC haute luminosité. Oct 2015. General Photo.
  - [14] Lyndon Evans and Philip Bryant. LHC machine. *Journal of Instrumentation*, 3(08):S08001–S08001, aug 2008.
  - [15] Tai Sakuma and Thomas McCauley. Detector and event visualization with SketchUp at the CMS experiment. *Journal of Physics: Conference Series*, 513(2):022032, jun 2014.
  - [16] A.M. Sirunyan et al. Performance of the CMS muon detector and muon reconstruction with proton-proton collisions at  $\sqrt{s}=13$  TeV. *Journal of Instrumentation*, 13(06):P06015–P06015, jun 2018.